Open Access Full Text Article

ORIGINAL RESEARCH

Engineered Hybrid Treg-Targeted Nanosomes Restrain Lung Immunosuppression by Inducing Intratumoral CD8+T Cell Immunity

Kalliopi Domvri[1], Savvas Petanidis[2,3], Paul Zarogoulidis[4], Doxakis Anestakis [5], Charalampos Charalampidis[5], Drosos Tsavlis[6], Haidong Huang[7], Lutz Freitag[8], Wolfgang Hohenforst-Schmidt[9], Dimitris Matthaios[10], Theodora Katopodi[2], Konstantinos Porpodis[3]

[1]Pulmonary Department-Oncology Unit, "G. Papanikolaou" General Hospital, Aristotle University of Thessaloniki, Thessaloniki, 57010, Greece; [2]Department of Medicine, Laboratory of Medical Biology and Genetics, Aristotle University of Thessaloniki, Thessaloniki, 54124, Greece; [3]Department of Pulmonology, I.M. Sechenov First Moscow State Medical University, Moscow, 119992, Russian Federation; [4]Third Department of Surgery, "AHEPA" University Hospital, Aristotle University of Thessaloniki, Thessaloniki, 55236, Greece; [5]Department of Anatomy, Medical School, University of Cyprus, Nicosia, 1678, Cyprus; [6]Department of Medicine, Laboratory of Experimental Physiology, Aristotle University of Thessaloniki, Thessaloniki, 54124, Greece; [7]Department of Respiratory & Critical Care Medicine, Changhai Hospital, Second Military Medical University, Shanghai, 200433, People's Republic of China; [8]Department of Pulmonology, University Hospital Zurich, Zurich, 8091, Switzerland; [9]Medical Clinic I, "Fuerth" Hospital, University of Erlangen, Fuerth, 91054, Germany; [10]Oncology Department, General Hospital of Rodos, Rodos, 85133, Greece

Correspondence: Savvas Petanidis, Department of Medicine, Laboratory of Medical Biology and Genetics, Aristotle University of Thessaloniki, Thessaloniki, 54124, Greece, Tel +30-2310-999-205, Fax +30-2310-999-208, Email spetanid@auth.gr

Introduction: Tumor immunotherapy is a key therapeutic paradigm for the treatment of several malignancies. However, in metastatic lung cancer, classical immunotherapy regimes are ineffective due to regulatory T cell (Treg)-related immunosuppression and tumor relapse.

Materials: To address this issue, we designed specific biocompatible Treg-targeted nanocarriers (NCs) as a model of immune-based nanotherapy, in order to target Treg-related immunosuppression in the lung tumor microenvironment. This is achieved through the combination of Dasatinib and Epacadostat integrated into biodegradable nanosomes which can inhibit and reverse Treg-supporting immunosuppression. Flow cytometry and immunofluorescence analysis, PET/CT scan, PTT/PA imaging and the Balb/c tumor model were used to explore the anti-tumor effect of Treg-targeted NCs both in vitro and in vivo.

Results: Findings reveal that NC treatment triggered substantial tumor cell apoptosis and drastically decreased tumor volume followed by downregulation of Ki-67 antigen expression, respectively. Drug circulation time was also increased as shown by biodistribution analysis accompanied by greater accumulation in lung and peripheral tissues. Intratumoral Th1 cytokines' expression was also increased, especially TNF-A, IL-12 by 42%, and IL-6 by 18% compared to PBS treatment. In addition, the presence of mature CD80+/CD86+dendritic cells (DCs) revealed T cell enrichment and a decline in MDSC infiltration and myeloid subsets. Interestingly, a significant decline of Gr/CD11b myeloid cell population in blood and tissue samples was also observed. This immune activation can be attributed to the enhanced PTT efficiency and tumor targeting ability of the nanospheres which under near infrared (NIR) exposure can prompt highly efficient tumor ablation. We also demonstrated their therapeutic efficacy against 4T1 metastatic breast cancer model. Additionally, the photothermal therapy in combination with PD-L1 checkpoint blockade therapy exerted long-term tumor control over both primary and distant tumors.

Discussion: Overall, our findings present a novel nano-enabled platform for the inhibition of Treg-dependent immunosuppression in NSCLC and provide a novel nanotherapeutic strategy for the treatment of metastatic neoplasia.

Keywords: Tregs, nanosomes, metastasis, immunosuppression, T cells

Introduction

Despite the recent advances in tumor immunotherapy, lung cancer (LC) remains the primary cause of cancer-related deaths worldwide and regardless of broad research endeavors, the survival statistics of LC patients are disappointing.[1,2] Critical role in the establishment of lung tumor immunosuppression play the regulatory T cells (Tregs).[3–5] Tregs or suppressor T cells are

immunosuppressive cells that regulate the immune response to self and foreign antigens and help prevent autoimmune disease.[6,7] Tregs as a subpopulation of CD4+T cells highly express the CD4 T cell co-receptor CD25 which is a component of the IL-2 receptor and the transcription factor fork head box P3 (FoxP3).[4,8,9] Treg cells are able to control not only T cells but also B cells, NK cells, dendritic cells (DCs) and macrophages via humoral and cell-to-cell contact mechanisms.[10–12] Tregs inside the TME play a substantial role in promoting tumor expansion via cancer cell remodeling, which triggers immunosuppression and subsequent metastasis.[13–15] Intratumoral Tregs allow malignant cells to bypass immune surveillance and reduce T-cell infiltration into tumor, restricting the clinical advantage of immunotherapy regimes.[16,17] In order to surmount this Treg-dependent immunosuppression and potentiate the immune antitumor responses, depletion or functional inhibition of Tregs in combination with current immunotherapy regimens is a valuable approach.

Dasatinib is a multikinase inhibitor that targets SRC family kinases (SFKs) and BCR/ABL kinases and is used for the treatment of chronic myelogenous leukemia (CML) and acute lymphoblastic leukemia (ALL).[18,19] Its antitumor mechanism is based on its ability to inhibit the nonreceptor tyrosine kinases SRC family, c-KIT, EPHA2 and PDGFRβ.[20,21] Dasatinib has been shown to inhibit the proliferation and function of CD4+/CD25+ regulatory T cells in peripheral blood and reverse T cell suppression.[22,23] Additionally, it has shown to enhance T effector cell function and promotes the expansion of T-cell repertoire in melanoma inducing growth arrest and apoptosis of these tumor cells in vitro.[24,25] In a similar approach, Epacadostat is an inhibitor of indoleamine 2,3-dioxygenase-1 (IDO1) that has been reported to promote the growth of effector T cells and NK cells, increase the number of CD86+ dendritic cells and reduce Treg expression.[26,27] The combinational treatment of Dasatinib and Epacadostat is able to inhibit Treg-derived tumor immunosuppression via Treg subset population depletion in the lung TME and reactivate immune responses.

On this basis, we have synthetically engineered specialized copper sulfide nanocarriers (CuS NCs) that enfold Epacadostat/Dasatinib (EPDA) complexes for efficient photothermal therapy against Treg-related immunosuppressive cells. Due to their exceptional near-infrared (NIR) optical absorption, the high photothermal conversion efficiency and the strong photoacoustic (PA) imaging, CuS nanospheres can successfully destroy residual tumor cells and prevent local cancer recurrence and metastasis.

Results reveal CuS/EPDA nano treatment to downregulate Ki-67 antigen expression followed by increased release of ROS radicals inside the lung epithelium. Increase in drug circulation time, as well as an improved accumulation in lung and peripheral tissues was detected through biodistribution analysis. Additionally, enhanced intratumoral Th1 cytokine expression was monitored, especially TNF-A, IL-12 and IL-6. Furthermore, the presence of mature CD80+/CD86+dendritic cells (DCs) revealed T cell activation followed by decreased MDSC infiltration and myeloid subsets were characterized by the reduction of Gr/CD11b cell population in blood and tissue samples. This phenomenon correlated with reduced activation-induced cell death (AICD) of T lymphocytes and an upregulation in infiltration of IFN-γ+CD8+ T cells. This immune activation cascade can be accredited to the enhanced PTT efficiency and tumor targeting ability of the nanospheres which under near infrared (NIR) exposure can prompt highly efficient tumor ablation. We also demonstrated their therapeutic efficacy against 4T1 metastatic breast cancer model. Additionally, the photothermal therapy in combination with PD-L1 checkpoint blockade therapy exerted long-term tumor control over both primary and distant tumors. Overall, our findings provide a novel nano-enabled platform for the inhibition of Treg-dependent immunosuppression in lung TME. This engineered nanovaccine can elicit an effective robust antitumor immunity against solid tumors by synergistically modulating the tumor microenvironment. Taken as a whole, these results reveal the central role of Treg-targeted nanoplatform for the precise targeting of lung immunosuppression and present new approaches for the treatment of metastatic NSCLC.

Methods
Synthesis of CuS/EPDA NCs

For the CuS NPs synthesis, 1000 mL of CuCl$_2$ (1 mmol) in aqueous solution and sodium citrate (0.68 mmol) was added in 1 mL of sodium sulfide solution (Na$_2$S,1M) under stirring at room temperature. Following five minutes resting time, the mixture was heated to 90°C and stirred at 1000 rpm for 4h until a dark green solution was obtained. Adjusting the stoichiometric ratio between CuCl$_2$ and Na$_2$S, resulted in selection of nanoparticles with peak absorption (980nm). Then, isolated CuS (30mg) were dispersed into 100 mL of PLGA-PEG-3000 (Mw = 3000) in ethanol solution (0.5 mg/ml^{-1}) and magnetic stirring was applied at 50°C.

Following PEGylation process (12h), the CuS NCs were centrifuged and rinsed with ethanol and ddH2O to remove the residual PEG. The resulted PEGylated CuS NCs were then dispersed into 10 mL of sodium acetate buffer (2M), followed by the addition of Epacadostat (10mg) and Dasatinib (10mg). After 24h, the resulting CuS/EPDA NCs were obtained by centrifugation, dispersed in PBS (pH7.4) and stored at 4°C.

Conjugation of Rhodamine B Isothiocyanate on CuS/EPDA NCs

For conjugation, centrifugation and redispersion of 5 mL of isolated CuS/EPDA NCs in 10 mL of MES buffer (20mM, pH 6.0) was performed. Next, in the mixture, RHB Isothiocyanate was added and gently stirred for 24h in the dark at room temperature. Finally, particles were repeatedly washed with distilled water several times to remove redundant Rhodamine B.

Cell Culture

Human epithelial lung adenocarcinoma A549 and H-1993 cells were obtained from the American Type Culture Collection (ATCC, Manassas, VA, USA) and were grown in DMEM (dulbecco's modified eagle medium) supplemented with 10% fetal bovine serum, 2mM L-glutamine, 1 mM sodium pyruvate, 100 U/mL penicillin and 100μg/mL streptomycin (Biochrom, Germany). The cell cultures were grown to confluence and maintained in a humidified atmosphere at 37°C and 5% CO2. Both A549 and H-1993 cells were incubated with fetal bovine serum-free medium for 24h prior to the experiments with the CuS and CuS/EPDA compounds.

Animals

Six weeks old male BALB/c mice were purchased from the Jackson laboratory (BarHarbor, ME) and were housed under pathogen-free environment with a 12h light/12h dark schedule and fed with an autoclaved diet and water ad libitum. For the establishment of orthotopic xenografts, suspended A549 luciferase cells ($2x10^6$) in 20mL of HBSS medium, were directly implanted into the upper region of the lungs. Mice were randomly divided into four groups three days after implantation. Three separate groups of mice (n = 8) were injected subcutaneously in lung section with CuS and/or CuS/ EPDA (2mg/kg body weight in 0.1mL PBS, once a day and 5 days per week for 8 weeks). Control mice (n = 8) were treated the same with vehicle (0.1mL PBS). In addition, distinct groups of mice (n = 8) were injected subcutaneously in lung section with Epacadostat and/or Dasatinib (2mg/kg body weight in 0.1mL PBS, once a day and 5 days per week for 8 weeks). After treatment, mice were sacrificed, lungs and lymph nodes were removed for bioluminescence imaging and quantification of tumor volume. Tumor volume (V) was determined by measuring length (L) and width (W) by a vernier caliper and calculated according to the following formula: $V = L \times W^2 / 2$. For imaging, mice were given ip injections of 150 mg of D-luciferin 10 min prior to imaging. All of the protocols were approved by the Aristotle University's Animal Research Committee in accordance with the NIH Guidelines for the Care and Use of Laboratory Mice.

^{18}F-FDG/PET Scans

For the ^{18}F-FDG PET/CT, the studies were performed before the start of the combined Daclizumab treatment (baseline PET/CT), after three cycles of combined treatment (interim PET/CT), as well as after completion of the combined administration (late PET/ CT). All patients underwent at least two PET/CT scans. An interim PET/CT scan was performed 4–6 weeks after first-line Daclizumab treatment. The PET/CT system (Biographm CT, S128; Siemens, Germany) with an axial field of view of 21.6cm with TruePoint and TrueV, operated in a three-dimensional mode, was used for the ^{18}F-FDG PET/CT studies. After an injection of about 3MBq of ^{18}F-FDG/kg/bw, patients rested for a period of about 60min. Emission images ranging from the base of the skull to mid-thigh were acquired for 2–3min per bed position. Processed images were displayed in coronal, transverse and sagittal planes. A low dose attenuation CT (120 kV, 30 mA) was used for attenuation correction of the PET data and for image fusion. All PET images were attenuation-corrected and an image matrix of 400×400 pixels was used for iterative image reconstruction. Iterative image reconstruction was based on the ordered subset expectation maximization algorithm with six iterations and 12 subsets.

Pharmacokinetics Analysis

For the pharmacokinetic analysis, blood kinetics were assessed by drawing 8–10 mL of blood from the tail veins of BALB/c mice at certain time intervals post-injection of the CuS/EPDA NCs. Each blood sample was dissolved in 1mL of lysis buffer and the blood concentration of the NCs was determined by fluorescence spectrum acquired using a Fluoromax 4 fluorometer.

The plasma, tumors, and various tissues were collected at 0, 0.5, 1, 2, 4, 6, 12, 24, 48, 72 and 96h after treatment. All the samples were stored at −80°C until further analysis.

Ex vivo Tissue Culture

Lung samples from consenting lung cancer (KRAS, chemoresistant) patients at the AHEPA Hospital Oncology unit were collected, transferred to research lab in cold media and processed in a sterile tissue culture hood (Supplementary Tables S1–S3). The culture protocol is modified based on previous studies[28,29] (Supplementary Methods).

Orthotopic 4T1 Breast Cancer Model

To set up the 4T1 orthotopic breast tumor model, 4T1 cells (6×10^4) were injected into the mammary fat pads of mice on the right side of the abdomen. Seven days later, 4T1 cells were injected into the left mammary fat pads of the mice to establish the bilateral tumor model. Anti-PD-L1 antibodies at the dose of 80μg/mouse were administered on days 1, 4, 6 and 8. The tumor volume was calculated according to the following formula: (width$^2 \times$length)/2. At the end of the experiment, mice were killed and tumors were excised, weighed and photographed.

Statistical Analysis

The results are expressed as mean±SD from at least three separate experiments performed in triplicate. The differences between groups were determined with a two-tailed Student's *t*-test or ANOVA using GraphPad software. The results represent the mean±SD of at least three independent experiments. Differences were considered statistically significant at $p < 0.05$. Statistically significant data are indicated by asterisks (*$p < 0.05$,**$p < 0.01$).

Ethics Approval and Consent to Participate

The study protocol conformed to the ethical guidelines of the Declaration of Helsinki and was approved by the Institutional Review Board and Ethics Committee of the AHEPA Hospital Medical School, Aristotle University of Thessaloniki.

In vitro generation of Tregs, MDSCs analysis, Immunofluorescence analysis, T-cell function assays, Transmission Electron Microscopy imaging, PTT/PA imaging and TUNEL/Annexin V apoptosis detection. Detailed methods and protocols are provided in Supplementary Methods file.

Results

Molecular Characterization of CuS/EPDA Nanocarriers

To allow efficient systematic administration and successful tumor accumulation, the construction of CuS/EPDA nanocarriers encapsulating Epacadostat/Dasatinib (EPDA) complexes was based on the solvent dialysis method. For that reason, PLGA-PEG, an FDA-approved polymer was employed due to its biodegradable and biocompatible nature and is extensively used as a nano-delivery vehicle of chemotherapy drugs (Figure 1A). The amphiphilic structure of this micelle protects the interior CuS core from oxidative damage which improves photothermal constancy and restrains the degradation rate of the nanocarriers in vivo. This nano configuration allows prolonged blood circulation and substantial penetration into tumors via the EPR effect. The obtained CuS/EPDA nanosomes display spherical morphology with an average diameter of 84±3.0 nm according to statistical AFM and dynamic light scattering (DLS) analysis (Figure 1B and C). The soluble mixture of CuS/EPDA nanosomes was stable for up to 72h in both PBS and 10%FBS with minor size discrepancies. The main characteristic of these nanosomes is the increased biocompatibility between Epacadostat and Dasatinib complexes. These molecules which are highly chemically compatible with each other guarantee increased biosafety and release both in vivo and in ex vivo applications (Figure 1D). The optical

characteristics of the CuS/EPDA NPs under UV-vis spectroscopy display a characteristic distinctive absorption peak at 960nm (Figure 1E).

Furthermore, the stable uniform spherical composition of the nanocarriers was confirmed by TEM images (Figure 1F) whereas the fluorescence emission spectrum is constant following incorporation of Rhodamine B (Figure 1G). Furthermore, FTIR spectroscopy was used to verify the conjugation of Epacadostat/Daclizumab complexes to CuS nanosomes (Figure 1H). Overall, these observations highlight the significance of CuS/EPDA NCs as ideal vehicles for delivering and releasing therapeutic drugs at tumor tissues.

CuS/EPDA Mechanism of Antitumor Immune Activation

In order to investigate the CuS/EPDA tumor targeting mechanism, the phototoxicity of CuS/EPDA nanocarriers towards metastatic cells was assessed. To facilitate this, we examined several concentrations of CuS/EPDA nanosomes, following incubation with highly aggressive H-1993 metastatic cells. For concentrations above $2mg/mL^{-1}$, cell viability of H-1993 cells, reduced considerably following co-staining by calcein AM and PI, indicating the prominent ROS production by CuS/EPDA nanocomplexes (Figure 2A). Next, we decided to explore the photothermal aptitude of CuS/EPDA nanocarriers under normal and hypoxic pH status. Consecutively, H-1993 and A549 cells were incubated with NCs, followed by laser irradiation with 970 nm laser ($1Wcm^{-2}$) for 10min and then cell viability was evaluated by CCK-8 assay (Supplementary Figure S1). Findings reveal an extensive reduction in H-1993 cell viability under physiological pH whereas increased cell viability rates were detected in
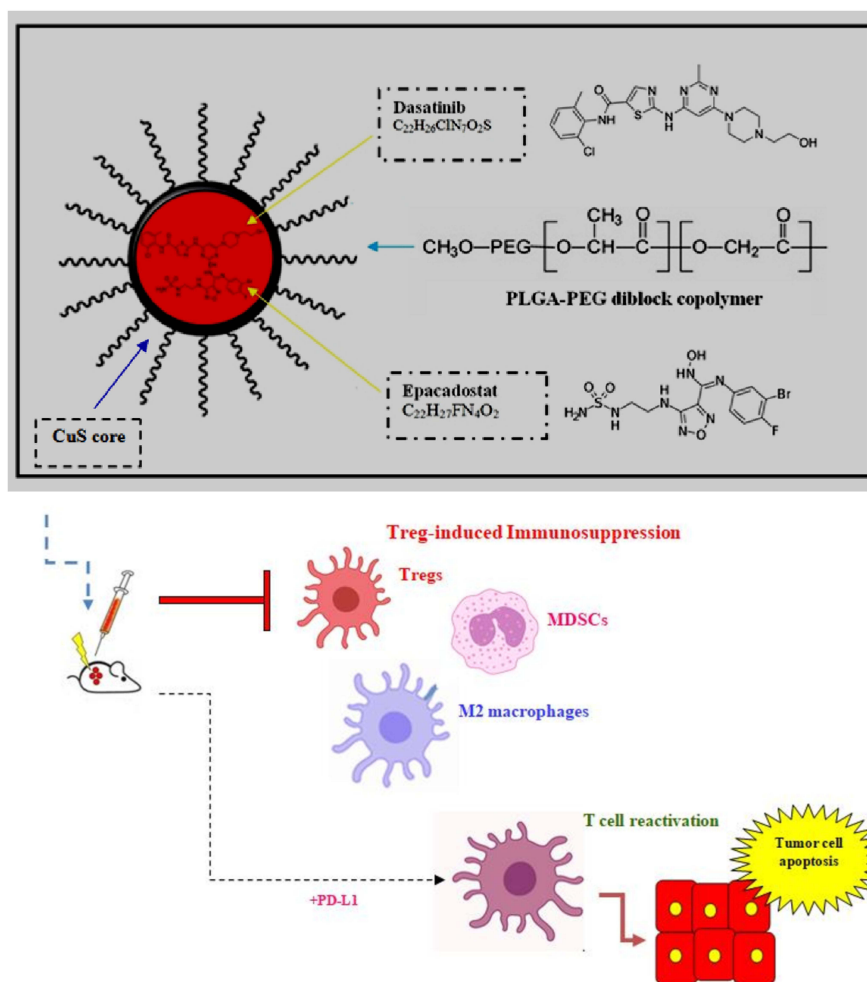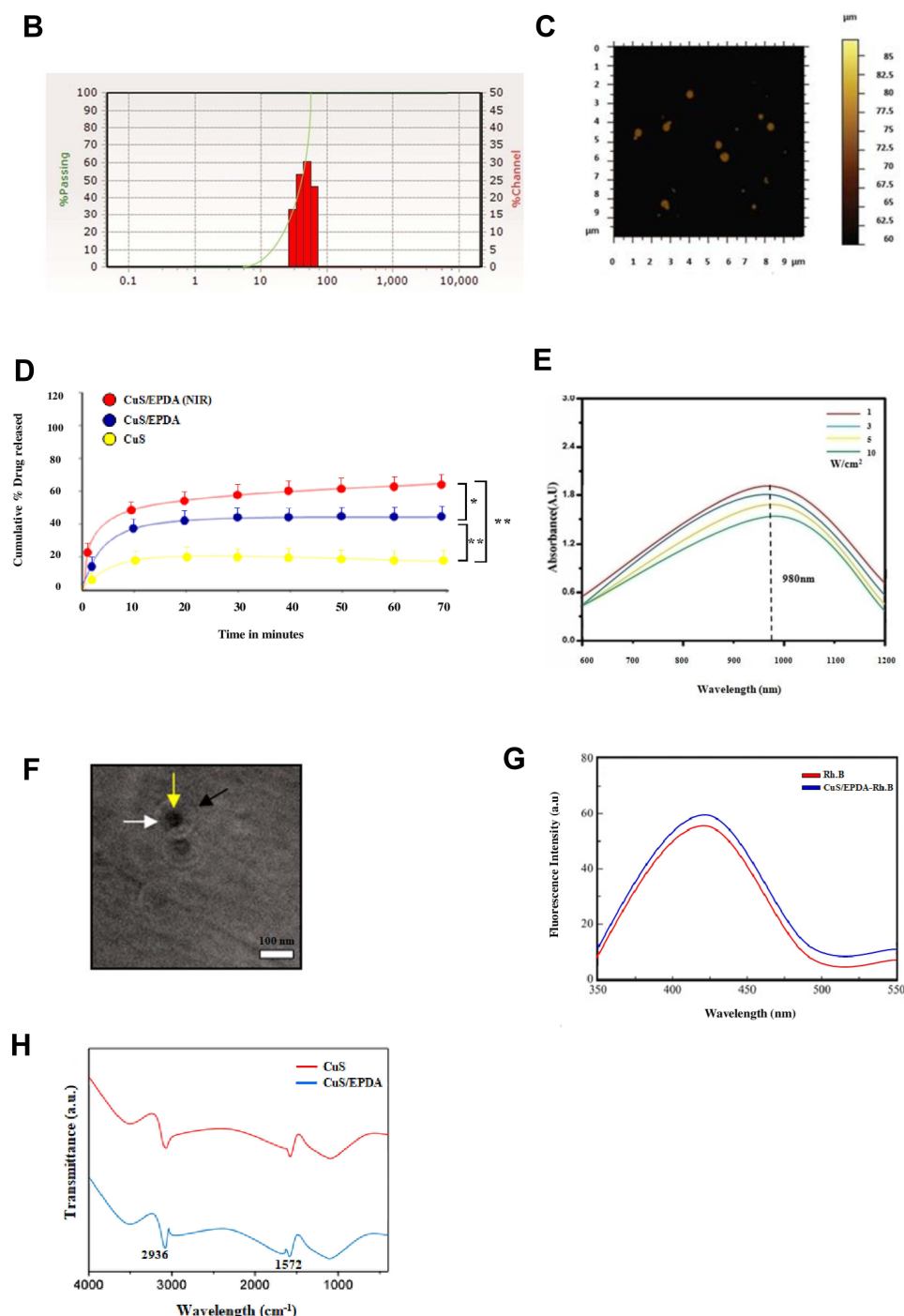

Figure 1 Continued.

Figure 1 Characterization analysis of CuS/EPDA nanospheres. (**A**) Graphic illustration of the CuS/EPDA NCs. (**B**) Size distribution analysis of CuS/EPDA NCs by dynamic light scattering (DLS) method. (**C**) Characteristic AFM images of NCs. (**D**) Drug release curves from CuS/EPDA NCs with or without NIR irradiation. (**E**) UV–vis absorbance spectra analysis. (**F**) Characteristic TEM image of the CuS/EPDA NCs (black arrow: PLGA-PEG, white: CuS core, yellow: epacadostat/dasatinib drug complex). The white arrow indicates the distinct dark CuS core within the nanocarriers. (**G**) The fluorescence emission spectra of CuS/EPDA NCs. (**H**) The FTIR spectra of CuS and CuS@EPDA. The results represent the mean±SD of three Independent experiments. Differences were considered statistically significant at p < 0.05. Statistically significant data are indicated by asterisks (*P < 0.05, **P < 0.01).

similar concentrations under hypoxic pH values (Figure 2B). In contrast, in A549 cells, cell mortality was vaguely augmented under acidic conditions in comparison with normal pH (Figure 2C). This mechanism can be credited to the inner core of the CuS/EPDA nanocomplexes which portrays high phototoxicity followed by the production and release of highly toxic hydroxyl radicals (–OH) in tumor stroma. To further analyze this effect of CuS/EPDA NCs phototoxicity in immune responses, we

measured the intracellular cytokine levels in NC-treated mice. Since the NCs display potent immune stimulatory properties, we assessed the levels of Th1 cytokines TNF-A, IL-6 and IL-12. Findings reveal an increase in IL-12 and TNF-a in the first 24h compared to upregulation of IL-6 in 72h post treatment (Figure 2D–F). Since dendritic cells (DCs) secrete the majority of cytokines in TME and are the main regulators of immune response via antigen presentation and T-cell stimulation, we decided to investigate their crucial role. For that reason, we measured the degree of DC maturation by the expression of the co-stimulatory molecules CD80 and CD86, which are important for T cell activation. Findings show an augmentation in mature DC levels in mice treated with CuS/EPDA and CuS NCs in comparison with the control groups (Figure 2G and H). To better analyze the degree of immune activation, we measured immunosuppression biomarkers in tumor tissues. Levels of arginase 1 (Arg1) and inducible nitric oxide synthase (iNOS) were constantly measured post CuS and CuS/EPDA incubation. Expression of both iNOS and Arg1 expression was significantly downregulated in the CuS (18% and 22% respectively) and CuS/EPDA groups (40% and 15% respectively) (Figure 2I and J). Furthermore, free radical ROS expression was extensively declined (Figure 2K), indicating the vital role of CuS/EPDA in restraining Arg1/iNOS-related immunosuppression via ROS inhibition.

Pharmacokinetic Analysis of CuS/EPDA Nanocarriers

To better comprehend the antitumor immune response of CuS/EPDA NCs, the photothermal capability of the CuS/EPDA NCs was evaluated in vitro by NIR irradiation. By using an infrared thermal camera, temperature changes were monitored and examined. Findings illustrate a punctual rapid increase in the surface temperature of CuS/EPDA nanosomes within the first 2 minutes of the observed time period (Figure 3A). These results indicate that CuS/EPDA NCs could efficiently convert the absorbed photons into heat and serve as photothermal agents for tumor ablation. Furthermore, this NIR-heating behavior of the
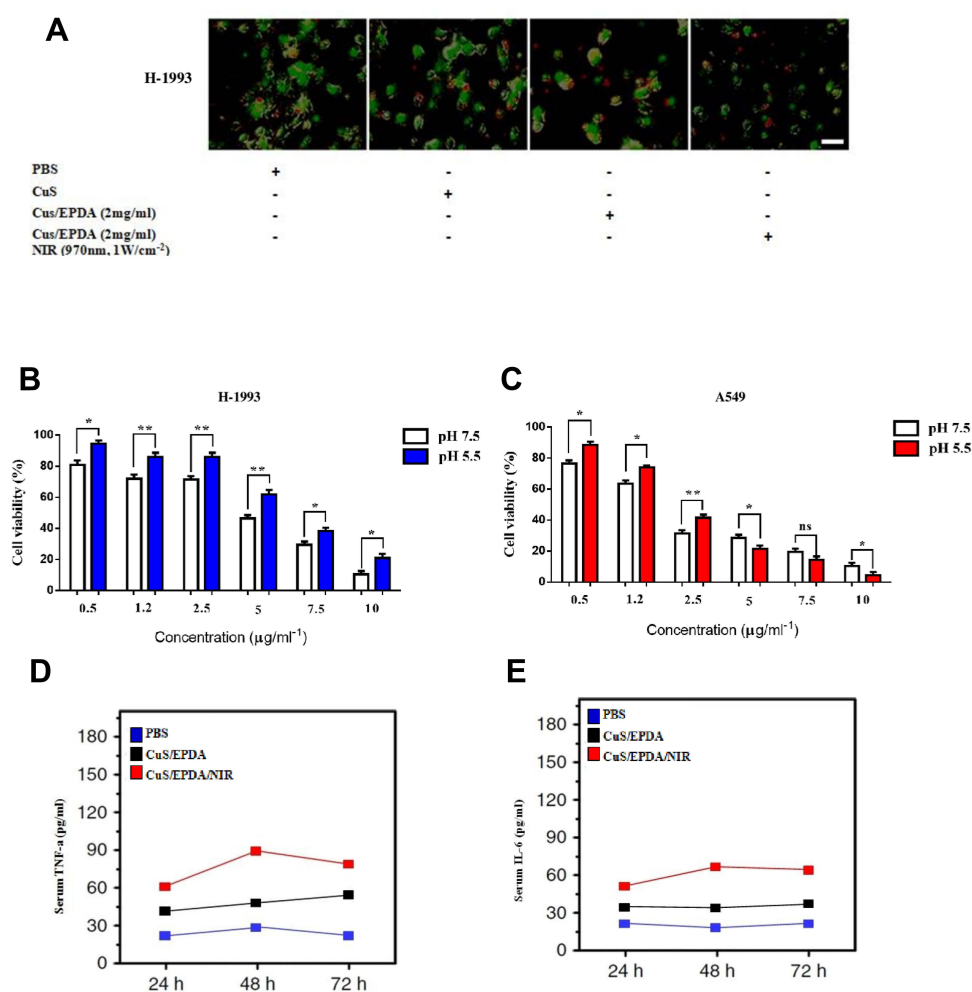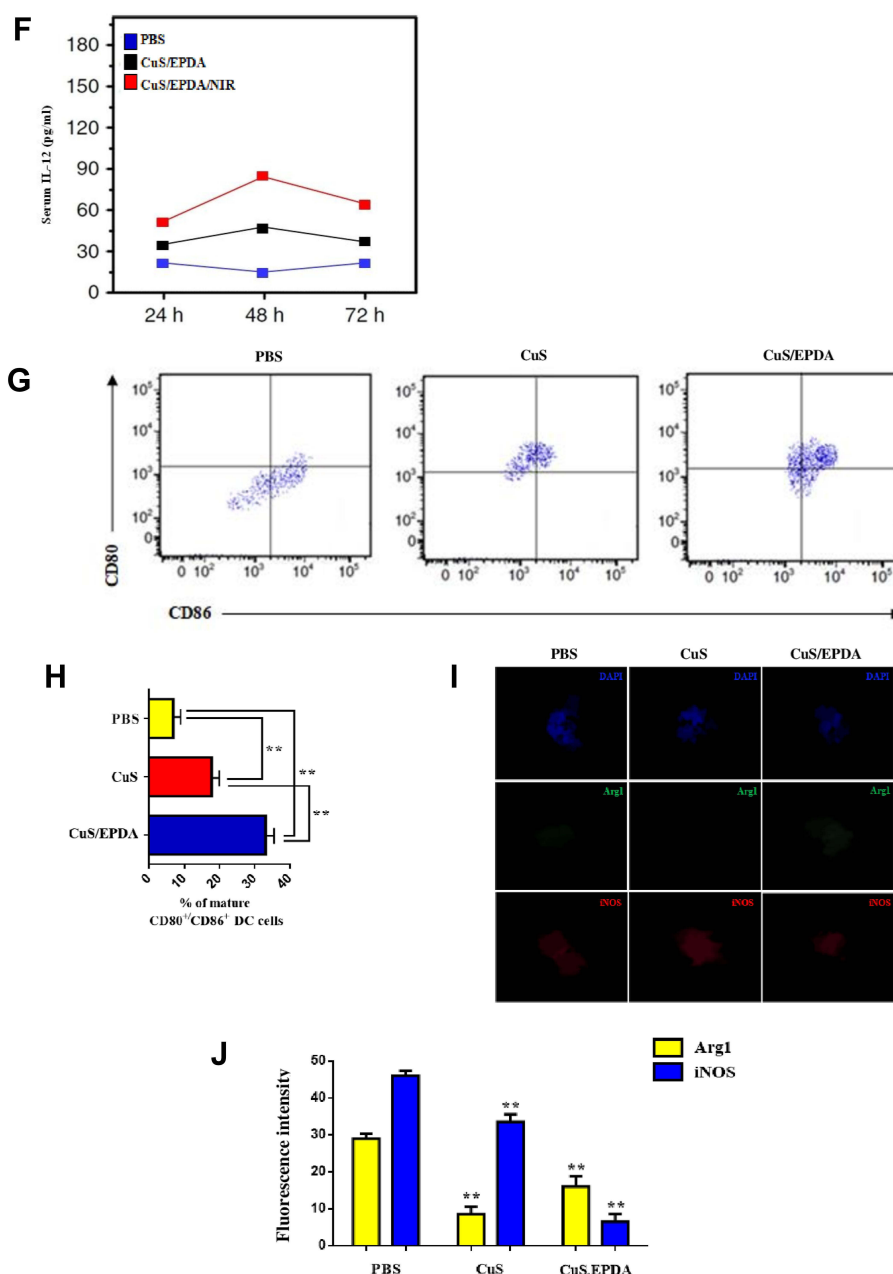

Figure 2 Continued.

Figure 2 Continued.

NCs was both concentration and time-dependent. We then performed Ki67 and CytoCalcein staining and data show that tumors treated with PTT in combination with CuS/EPDA NCs exhibit minimal proliferation along with substantial late apoptosis and necrosis (Figure 3B). Blood circulation analysis of the NCs in the blood of the A549 tumor-bearing BALB/c mice shows a circulating half-life of 3.17h in blood flow denoting the CuS/EPDA enrichment in blood through the EPR effect (Figure 3C). Additionally, biodistribution analysis reveals a greater accumulation of nanoparticles in spleen, lungs and liver than in kidney, heart and brain in NC-treated mice (Figure 3D). Moreover, the eliminating rate constants of CuS/EPDA NCs were −0.412 and −0.017μg/mL^{-1}per hour, for the first stage and second stage, respectively. The shifting time interval between the two stages was 3.18h (Figure 3E and F). This phenomenon can be attributed to the extended long-term biostability of the CuS/EPDA NCs in PBS, where they maintain their rigidity and solidity (Figure 3G). On the contrary, blood kinetics analysis in BALB/c mice reveals that CuS/EPDA NCs are detected in blood circulation for a significantly longer time compared with epacadostat. Interestingly, NCs exhibit improved T1/2 and increased area under curve (AUC), and Cmax opposed to epacadostat (Table 1). However, both

K

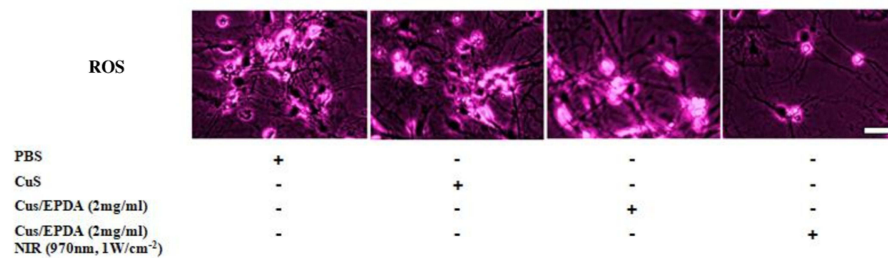|				
PBS	+	-	-	-
CuS	-	+	-	-
Cus/EPDA (2mg/ml)	-	-	+	-
Cus/EPDA (2mg/ml) NIR (970nm, 1W/cm⁻²)	-	-	-	+

Figure 2 CuS/EPDA tumor targeting mechanism. (**A**) Cell viability assay of lung metastatic H-1993 cells after treatment with CuS (2mg/mL) or CuS/EPDA (2–4mg/mL) for 4h (Scale bar, 20 μm). (**B** and **C**) cytotoxicity evaluation of CuS/EPDA NCs in H-1993 and A549 cells under neutral or hypoxic pH. Cells were treated with CuS/EPDA NCs (0.5–10μg/mL⁻¹) for 4h. Data represent the mean±SD of three independent experiments (*P < 0.05; **P < 0.01). (**D–F**) Flow cytometry analysis of intracellular cytokines TNF-A, IL-6 and IL-12 levels in NC-treated mice. Serum from mice was isolated 48–72h following treatment. Data represent the mean ±SD of three independent experiments. (**G** and **H**) DC maturation analysis using flow cytometry after staining with CD11c, CD80 and CD86. Data represent the mean ±SD of three independent experiments (**P < 0.01). (**I** and **J**) Immunofluorescence staining of immunosuppression biomarkers iNOS and Arg1 in tumor tissues after CuS and CuS/EPDA incubation. Confocal microscopy images of Arg1 (green). iNOS labeled cells (red) and DAPI (blue). Images were captured using Carl Zeiss fluorescence confocal microscope. Data represent the mean±SD of three independent experiments (*P < 0.01). (**K**) Intracellular ROS assay (Deepred, ab186029, Abcam) of lung metastatic H-1993 cells after treatment with CuS (2mg/mL) or CuS/EPDA (2–4mg/mL) for 4 h (scale bar, 20 μm). Differences were considered statistically significant at p < 0.05. Statistically significant data are indicated by asterisks.

clearance (Cl) and distribution volume (Vd) were significantly reduced over epacadostat. Combined values of clearance and distribution volume determine the half-life of CuS/EPDA nanosomes.

Inhibition of Treg-Induced Immunosuppressive Signaling

To verify the photothermal therapeutic efficacy of CuS/EPDA and evaluate their activity in vivo, we administrated A549-bearing BALB/c mice with CuS/EPDA NCs intratumorally in order to examine their therapeutic capability. Since, both myeloid cells and macrophages play a key role in metastatic potential, we evaluated their levels post NCs exposure. Growing evidence indicates that macrophage activity and performance is vastly regulated by myeloid cells, especially myeloid-derived suppressor cells (MDSCs) which are accountable for the intratumoral heterogeneity in lung cancer. Relative infiltration rate of monocytic MDSC subsets in M1/M2 macrophage regions is considerably reduced after NCs administration (Figure 4A and B). The expression levels of M2 macrophage markers (CD68+/CD163+) before and after treatment with CuS/EPDA NCs were also assessed (Supplementary Figure S2). Monitoring of MDSCs infiltration started three days post implantation. MDSC infiltration was evaluated by the presence of gMDSC (Gr−/CD11b−) and mMDSC (Gr−/CD11b+). Next, we determined the expression of tumor-infiltrating FoxP3⁺Tregs and the ratio of CD8⁺T/Tregs (Figure 4C–E). Treatment with NCs reduced the accumulation of intratumoral Tregs and enhanced tumor-infiltrating T cells and activated CD8+ T cell levels. Specifically, findings show downregulation of tumor-infiltrating FoxP3⁺CD4⁺Tregs followed by an increase in the ratio of CD8⁺T/Tregs (Figure 4C–E). In correlation with the increased CD8⁺T expression, the percentage of TUNEL positive cells was considerably enhanced by the treatment, suggesting that CuS/EPDA induces apoptosis (data not shown). Data also reveal that activation of CD8⁺ T cell subsets was accompanied by high frequency of IFN-γ⁺CD8⁺T cells in lung tissues (Figure 4F and G). Taken together, these findings verify the ability of CuS/EPDA nanosomes, to elicit a potent immune response by inhibition of the Treg-induced immunosuppressive mechanism.

In vivo Inhibition of Primary and Metastatic Tumors

To better evaluate the therapeutic capacity of CuS/EPDA, an A549-mouse lung cancer tumor model was employed. To support this, we investigated the in vivo performance of NCs in the treatment of primary and secondary metastatic tumor after surgery in A549-tumor bearing mice. During the experimental procedure, two diverse doses (5,10mg/kg⁻¹) of CuS/EPDA NCs were employed. When tumor volume reached 200mm³, mice were randomly divided into groups and received intratumoral (IT) injections of PBS, CuS and/or CuS/EPDA NCs. Serial assessment of tumor volume exhibited considerable tumor reduction in the CuS/EPDA group in comparison with PBS and CuS group treatments (Figure 5A and B). Compared with CuS group, CuS/EPDA treatment resulted in ~37% tumor growth inhibition, due to enhanced tumor accumulation via the EPR effect.
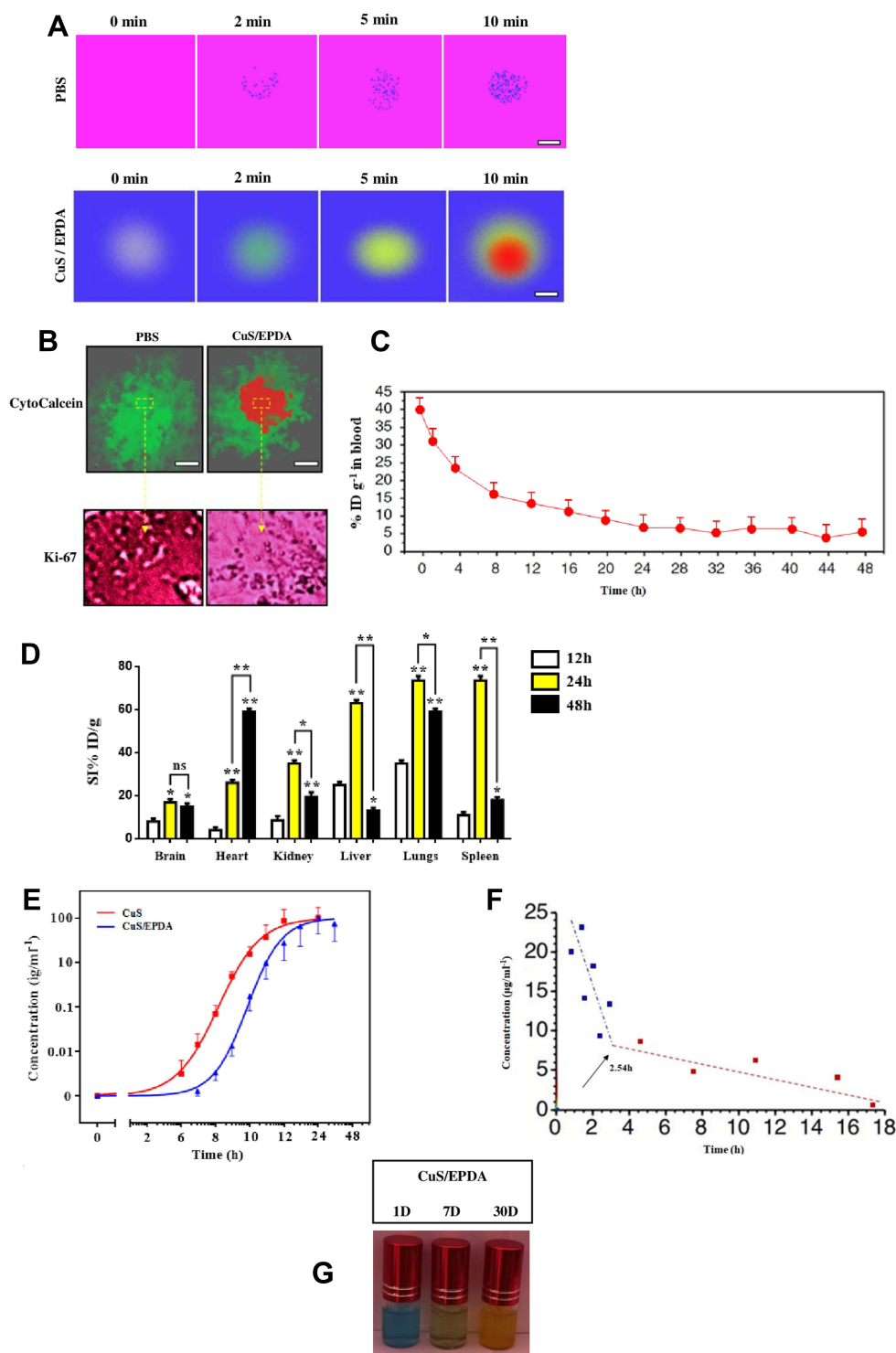
Figure 3 Pharmacokinetics and biodistribution analysis. (**A**) IR thermographic images of the CuS/EPDA nanosomes dispersed in PBS and irradiated with the 970 nm laser (1Wcm^{-2}) for 10 min (scale bar, 50 nm). (**B**) Ki67 and Cyto Calcein staining of the intravenously injected CuS/EPDA NCs in BALB/c mice. Images were captured using Carl Zeiss fluorescence confocal microscope. Data represent the mean±SD of three independent experiments (Scale bar, 100 μm). (**C**) Blood circulation curve of the intravenously injected CuS/EPDA NCs in BALB/c mice. (**D**) Quantitative biodistribution analysis of CuS/EPDA NCs in BALB/c mice by measuring the Cy5. 5 fluorescence intensity in major organs at different time points post-injection. Data represent the mean±SD of three independent experiments. Statistically significant data are indicated by asterisks (*P < 0.05, **P < 0.01, ns, not significant). (**E**) Quantitative concentration analysis of CuS and CuS/EPDA NCs in tumor area by measuring the Cy5.5 fluorescence intensity at different time points post-injection. (**F**) Eliminating rate curve of intravenously injected CuS/EPDA NCs according to the concentration (C) over time (T) relationship. The blue and red indicators represent the first and the second time points respectively. (**G**) Stability of CuS/EPDA NCs after air exposure for 1–30 days. The NCs were dispersed in PBS and stored in room temperature for different periods of time.

Table 1 Detailed Pharmacokinetic Analysis of CuS/EPDA NCs in Blood

Blood Pharmacokinetics Analysis of CuS/EPDA NCs.					
Groups	$T_{1/2}$ (h)	AUC (µg/h/mL)	Cmax (µg/mL)	CL (mL/h/kg)	Vd (mL/kg)
CuS/EPDA	3.547	38.27	12.56	2.86	21.52
Epacadostat	1.620	11.42	8.19	31.74	68.05

Note: The results represent the mean±SD of three independent experiments.

Remarkably, a subsequent in vivo metastatic assay revealed a significant decrease in the number of lymph node metastatic foci in CuS/EPDA group versus the PBS and CuS groups (Figure 5C and D). Tumor sections from CuS/EPDA-treated mice showed a considerable decrease in Ki-67 fluorescence intensity followed by elevated TUNEL fluorescence intensity, indicating apoptosis induction by the NCs (data not shown). Furthermore, tumor analysis data reveal that mice administered with NCs display a distinctly delayed tumor progression followed by high level of survival percentage. Specifically, survival statistics reveal that the CuS/EPDA-treated mice had long survival rate in comparison with control and CuS groups. In particular, mice injected with CuS alone had a significantly shorter median overall survival (OS) following tumor implantation (42 days) compared to mice injected with CuS/EPDA NCs (median OS, 58 days) (Figure 5E). To further evaluate the NCs tumor suppression efficacy, intravenous administration of NCs was performed in A549-tumor bearing mice. Results analysis based on relative tumor volume assessment revealed widely advanced rates of tumor reduction for CuS/EPDA treatment in relation to controls (Figure 5F and G). Equally, depletion of Ki-67 antigen expression and tumor volume shrinkage in NCs-treated groups could be also observed. Remarkably, xenografted tumor was reduced by 72% after 14 days of treatment and there was no recurrence, which further confirmed the excellent therapeutic efficacy of the designed NCs.

CuS/EPDA NCs Inhibit Activation-Induced Cell Death (AICD) of T Lymphocytes

Since Tregs trigger the establishment of T cell dysfunction, we decided to examine the effect of CuS/EPDA nanosomes in the immunological elimination or activation-induced cell death (AICD) of T lymphocytes which can be used by tumor cells to escape immune detection. This type of signal-induced programmed cell death is caused by the attachment of Fas ligands (FasL) to Fas receptor (CD95) triggering immune activation. Cell analysis revealed that the rate of AICD positive cells among $CD4^+/CD8^+$T cells was decreased significantly post CuS/EPDA administration (Figure 6A and B). To better evaluate this effect of Tregs in vivo, we tested the antitumor mechanism of Treg inhibition in a BALB/c mouse model. The percentage of $AICD^+$ cells from mice post CuS/EPDA treatment declined dramatically (Figure 6C). Tumor assessment analysis exhibited a substantial decrease in FasL, NFAT1 and in lung tumor volume of EPDA-treated mice compared to vehicle treated mice (Figure 6D). Furthermore, the percentage of $AICD^+$ cell population correlated with the infiltrating CD8 T cell ratio (R = 0.52) (Figure 6E). Next, we performed tumor evaluation where orthotopic growth of lung tumors was monitored weekly by bioluminescence imaging. The biodistribution of EPDA NCs was also evaluated and a high accumulation of nanosomes in the orthotopic tumor model was monitored. Bioluminescence analysis showed a significant decrease in the lung tumor volume of CuS/EPDA-treated mice compared to control (Figure 6F and G). To further validate tumor-infiltration photoacoustic (PA) imaging was employed to better inspect the NCs targeting ability in vivo. Interestingly, signal intensity was found to be thoroughly dependent on CuS/EPDA concentration in PA signals at 970nm (Figure 6H and I). To better understand this effect, we applied NIR exposure to CuS/EPDA solution at concentrations above 0.4 mgmL^{-1}. Findings, show a rapid temperature raise from 18.2°C to 62.7°C in 180 s. After centrifugation (1min), temperature was raised up to 70°C and remained stable without compromising the photothermal efficiency (Figure 6J). This also verifies that the signal intensity is highly dependent on the concentration of CuS/EPDA solution. To better understand the clinical effect of Treg inhibition in vivo, we used the FDA-approved drug Daclizumab and monitor its effect on selected Kras metastatic patients (Stage IV) using ^{18}F-FDG PET imaging. We noticed a high aggregation of the drug in lung lesions and a large proportion of the iv–injected Daclizumab was enriched in the tumor tissues through the EPR effect. Additionally, comparative ^{18}F-FDG PET imaging confirmed the lower tumor burden in
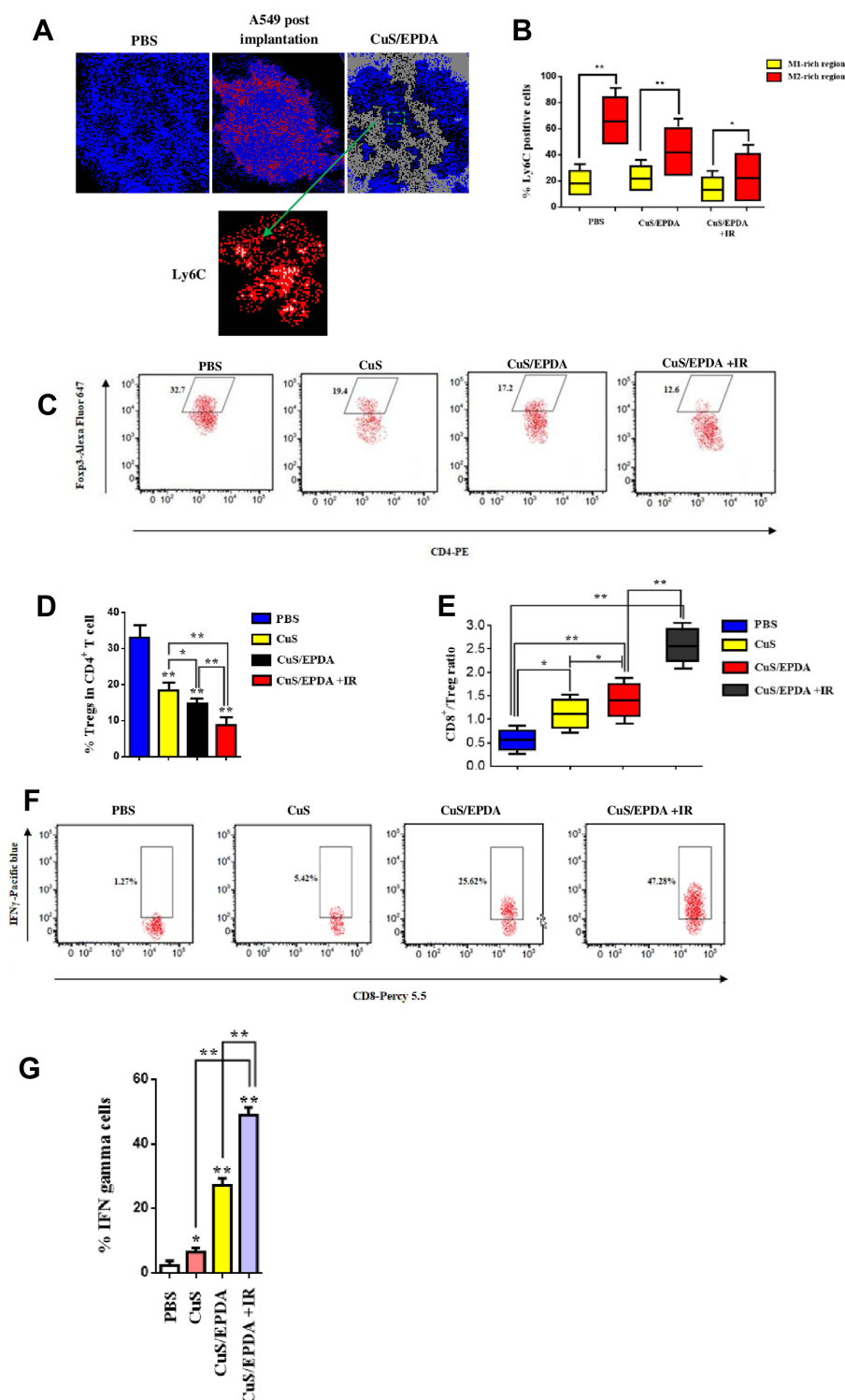
Figure 4 Assessment of intratumoral immune responses in vivo. (**A**) Infiltration of monocytic MDSC (Ly6C) subsets in M1/M2 macrophage regions post treatment with CuS/EPDA NCs. (**B**) Percentage of Ly6C^{+} infiltrated cells. Data represent the mean±SD of three independent experiments. Differences were considered statistically significant at p < 0.05. Statistically significant data are indicated by asterisks (*P < 0.05, **P < 0.01). (**C**) Expression analysis of tumor-infiltrating FoxP3^{+} Tregs in mice following treatment with CuS/EPDA NCs. (**D**) Percentage of Treg cells in CD4^{+} T cell population. The results represent the mean± SD of three independent experiments. Differences were considered statistically significant at p < 0.05. Statistically significant data are indicated by asterisks (*P < 0.05, **P < 0.01). (**E**) The CD8^{+}T/Tregs ratio analysis of the intravenously injected CuS/EPDA NCs in BALB/c mice. Statistically significant data are indicated by asterisks (*P < 0.05, **P < 0.01). (**F** and **G**) Expression analysis of IFN-γ^{+} CD8^{+} T cells in lung tissues following treatment with CuS and CuS/EPDA NCs. Data represent the mean±SD of three independent experiments. Differences were considered statistically significant at p < 0.05. Statistically significant data are indicated by asterisks (*P < 0.05, **P < 0.01).
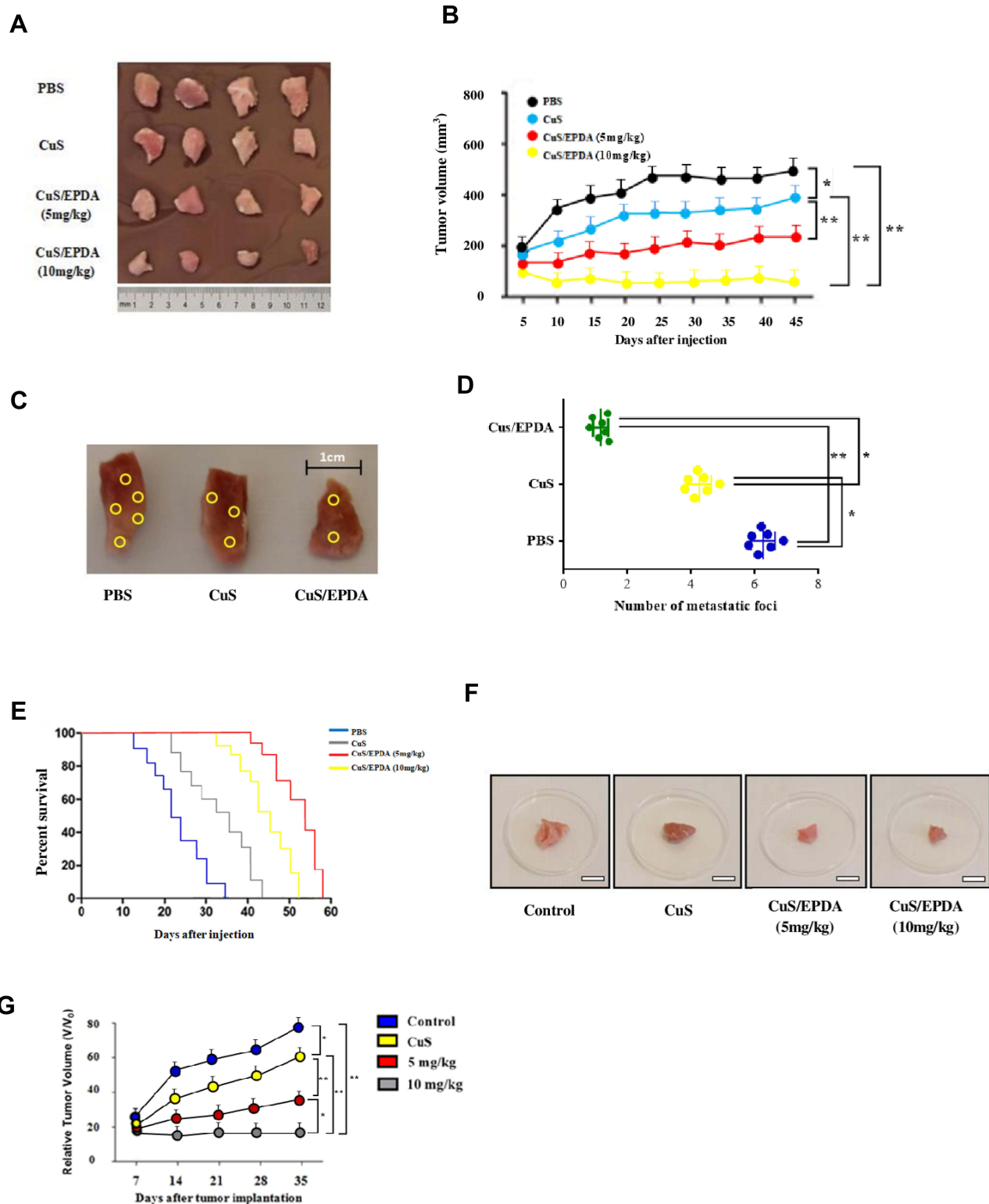
Figure 5 In vivo therapeutic efficacy against A549 tumor xenografts. (**A**) Characteristic photos of excised tumors from mice after treatment with CuS and CuS/EPDA NCs (5–10 mg/kg). (**B**) Comparative tumor volume assessment of A549 tumor bearing mice following treatment. (**C**) In vivo metastatic analysis of lymph node metastasis from control and CuS/EPDA NC-treated groups. Images showed representative lymph node metastatic foci highlighted in yellow color from different groups. (**D**) Statistical analysis of the number of metastatic foci of each group. (**E**) Survival rates of tumor-bearing mice after a 60-day tumor challenge in each group. Data were given as the mean ± SD (n = 6). Mean values and error bars are defined as mean and SD, respectively. (**F**) Representative photographs of excised tumors from mice after intravenous treatment with CuS/EPDA NCs (scale bar,1 cm). (**G**) Relative tumor volumes (V/V0) of A549 tumor bearing mice following intravenous administration. Data represent the mean±SD of three independent experiments (*P < 0.05; **P < 0.01).

A

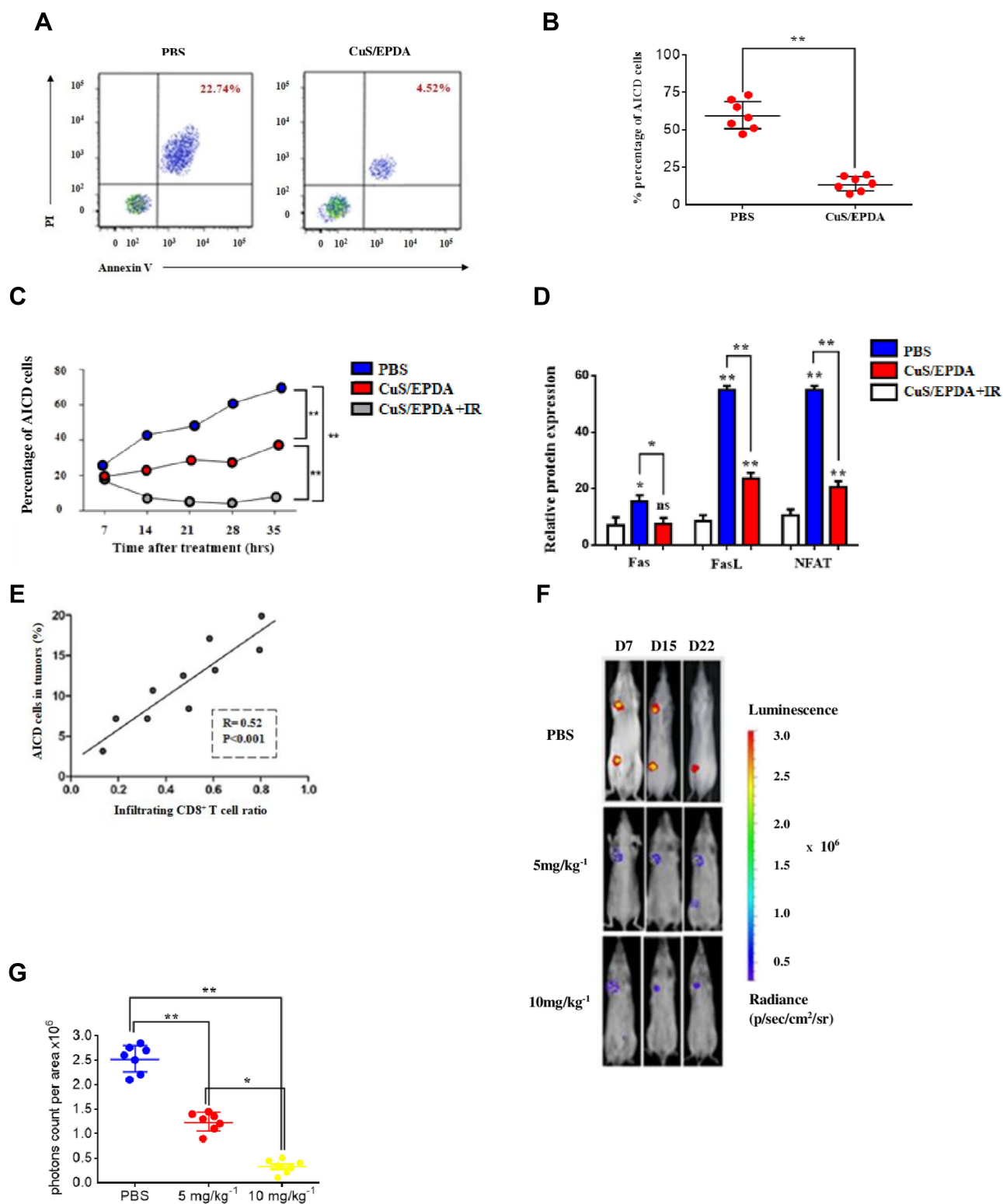**B**

C

D

E

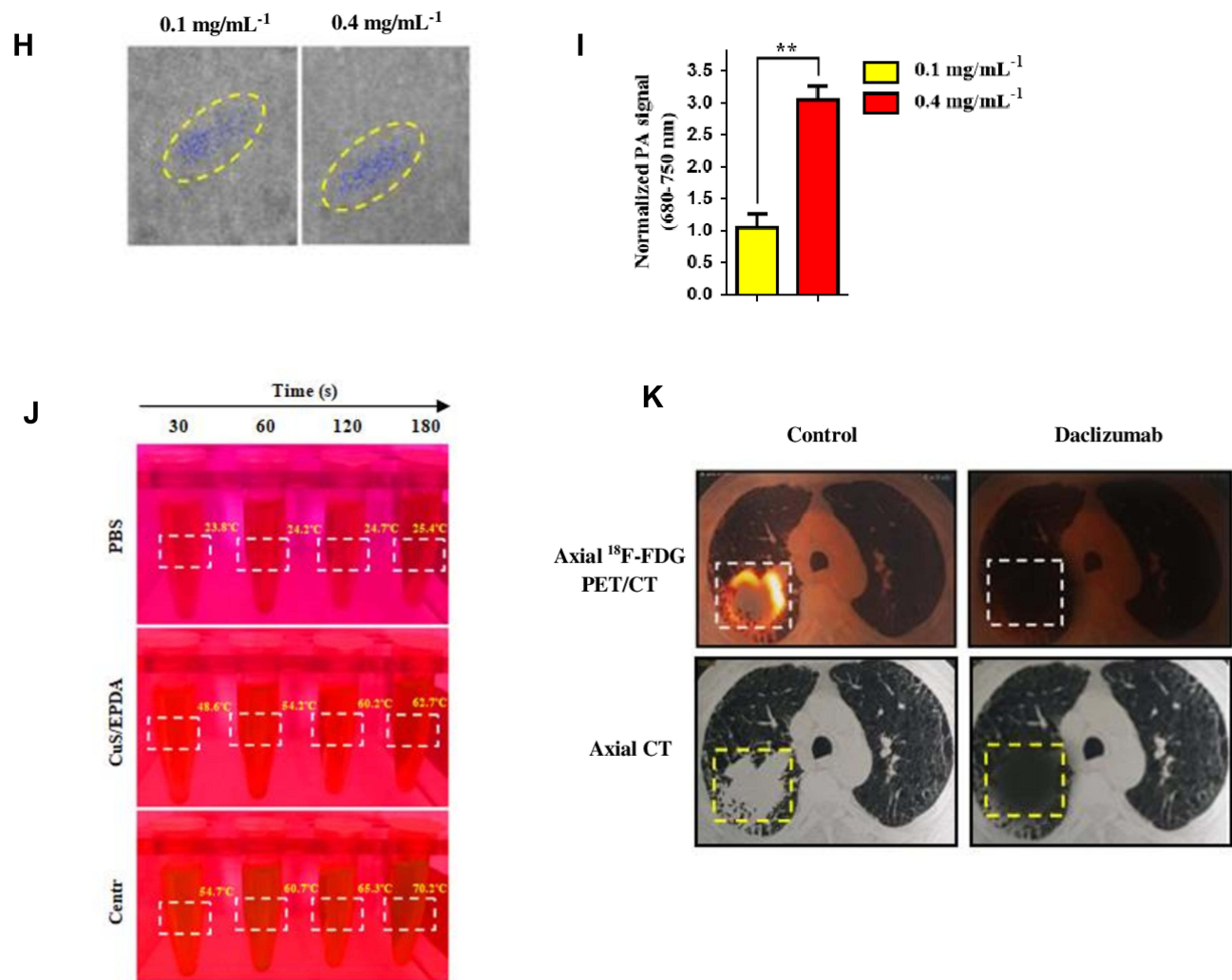
F

G

Figure 6 Continued.

Figure 6 Assessment of intratumoral immune responses in vivo. (**A**) Flow cytometry analysis of propidium iodide (PI) and annexin V staining of CD4^{+} T cells activated by CD3 and CD28 antibodies post CuS/EPDA administration. The CD4^{+} T cells were isolated from PBMCs following centrifugation. (**B**) Percentage of apoptotic AICD^{+} cells in relation to Treg expression. The results represent the mean±SD of three independent experiments (**P < 0.01). (**C**) Percentage analysis of AICD^{+} cells from mice after treatment with CuS/EPDA or CuS/EPDA+IR. Data represent the mean±SD of three independent experiments (**p < 0.01). (**D**) Relative protein expression of Fas, FasL and NFAT1 in CuS/EPDA-treated BALB/c mice in comparison with control (PBS). The results represent the mean±SD of three independent experiments (*P < 0.05; **P < 0.01). (**E**) Graph showing positive correlation between AICD^{+} cells and Infiltrating CD8^{+} T levels. The results represent the mean±SD of three independent experiments. (**F**) Bioluminescence imaging of mice from control (PBS) and CuS/EPDA NC-treated groups. (**G**) The bioluminescence values (photons/sec/cm^2/sr) were quantified for each group of mice and mean values±SE were plotted. The results represent the mean±SD of three independent experiments (*P < 0.05; **P < 0.01). (**H**) Photoacoustic imaging of CuS/EPDA NCs in PBS buffer with different concentrations (0.1, 0.4 mg/mL^{-1}). The highlighted yellow line indicates the isolated PA signal of the CuS/EPDA NCs. (**I**) The relative intensity of the PA signal at 680–750 nm. The results represent the mean±SD of three independent experiments (**P < 0.01). (**J**) Infrared thermal imaging of CuS/EPDA NCs and PBS with NIR irradiation (980nm, 1 Wcm^{-2}). The results represent the mean±SD of three independent experiments. (**K**) ^{18}F-FDG PET imaging shows the primary tumor in lung cancer patients before and after daclizumab (CD25 inhibitor) treatment.

Daclizumab-treated patients in relation to control groups. Furthermore, ^{18}F-FDG PET revealed noticeable tumor size differences between the treated and untreated groups (Figure 6K).

Notably, this verifies the crosstalk between Treg-related immunosuppression and tumor propagation. This perception has extensive prospective for clinically translatable cancer theranostics in applications such as tumor treatment, diagnosis and drug delivery.

CuS/EPDA Inhibits Growth of Metastatic Breast Cancer in Mice

To evaluate the therapeutic potential of CuS/EPDA in a more advanced tumor phenotype and evaluate their compatibility with current immunotherapy regimens, we employed a triple negative breast cancer 4T1 tumor model. At first, 4T1-luc cells were orthotopically implanted in the mammary fat pad of BALB/c mice. Following tumor formation (≥200mm^3), mice were intravenously injected with CuS, CuS/EPDA NCs and/or IR treatment.
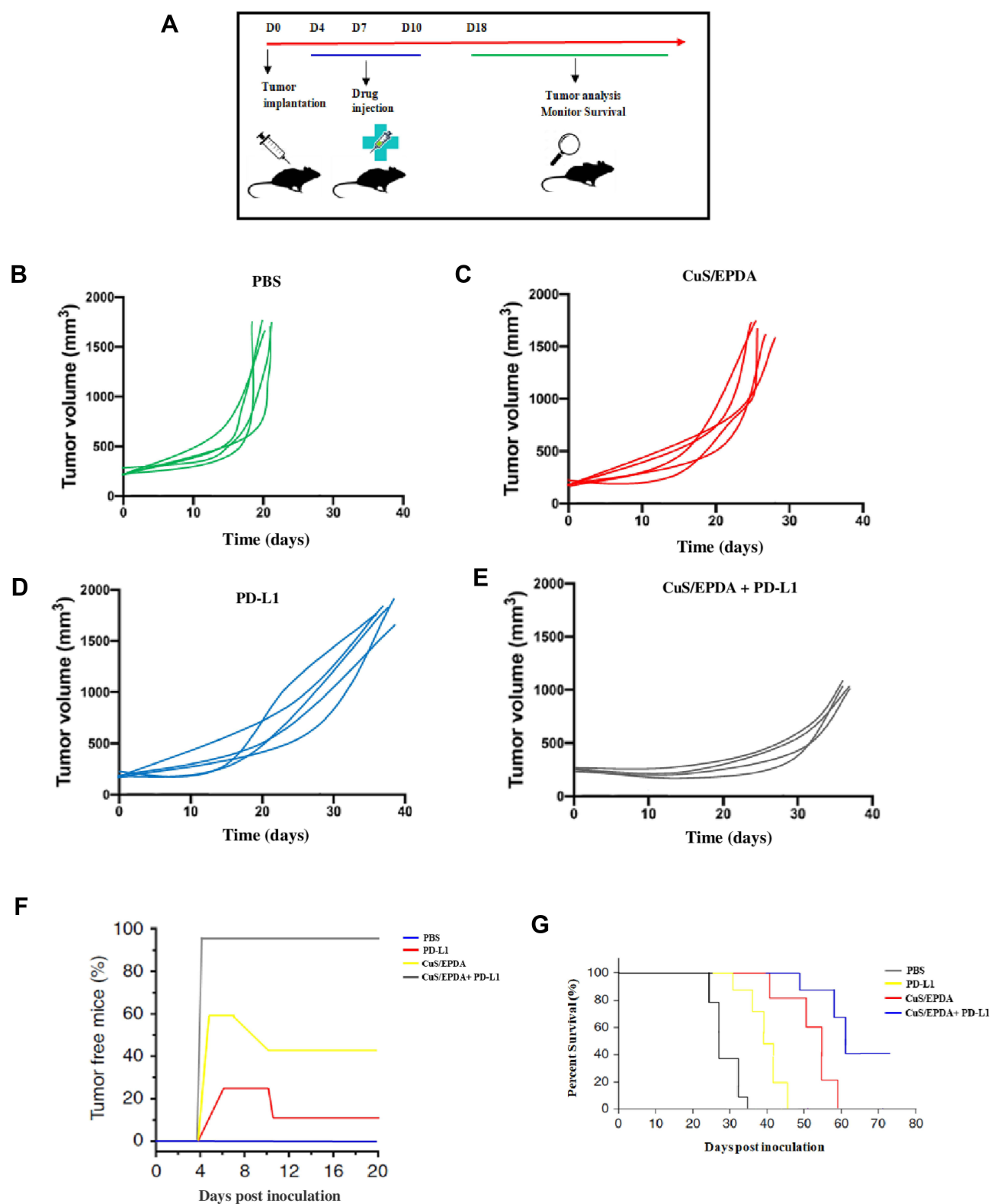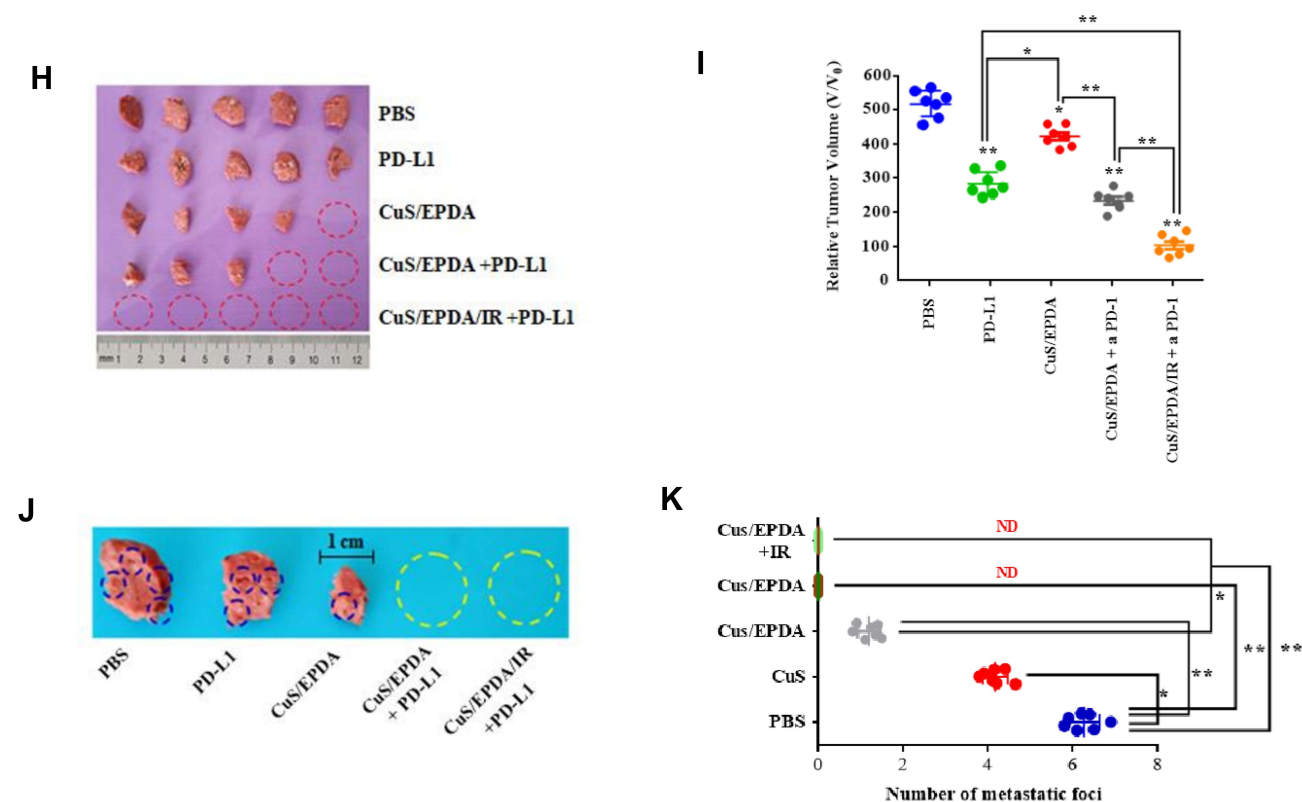
Figure 7 Antitumor effect of CuS/EPDA NCs plus anti-PD-L1 immunotherapy in 4T1 orthotopic tumor model. (**A**) Schematic illustration showing the treatments schedule in 4T1 mouse model. (**B–E**) Individual tumor growth kinetics in different groups. (**F**) Percentage rate of tumor-free mice during the treatments. (**G**) Morbidity-free survival of mice after the indicated treatment. The results represent the mean±SD of three independent experiments (**P < 0.01). (**H**) Representative photographs of excised tumors from mice after intravenous treatment with CuS/EPDA and anti-PD-L1 immunotherapy. (**I**) Relative tumor volumes (V/V0) of A549 tumor bearing 4T1 mice following intravenous administration. Data represent the mean±SD of three independent experiments (*P < 0.05; **P < 0.01). Differences were considered statistically significant at p < 0.05. (**J**) In vivo metastatic analysis of lymph node metastasis from CuS/EPDA and anti-PD-L1 immunotherapy-treated groups. Images showed representative lymph node metastatic foci highlighted in blue color from different groups. Yellow color represents no detected foci. (**K**) Statistical analysis of the number of metastatic foci of each group. Data represent the mean±SD of three independent experiments. Statistically significant data are indicated by asterisks (*P < 0.05, **P < 0.01, ND, not detected).

For the in vivo experiments, the treatment strategy was the same as the aforementioned protocol and is analytically described (Figure 7A). CuS/EPDA NCs or anti-PD-L1 alone failed to delay the growth of the primary tumors and survival rates, indicating the presence of strong immunosuppression that hinders therapeutic efficacy. However, co-treatment of CuS/EPDA NCs with anti-PD-L1 extensively inhibited the growth of both primary and metastatic tumors compared to PBS or single treatments (Figure 7B–E). Specifically, combination treatment resulted in 64% inhibition of tumor growth, whereas the percentage of tumor-free mice increased significantly to 25% (Figure 7F and G). Similar combination with photothermal therapy resulted in a 70% tumor-free rate and a 97% tumor growth inhibition (Figure 7H and I). Unexpectedly, repeated combination treatments resulted in the complete eradication of all tumors in each of the treated mice on three cases (Figure 7G). These findings confirm that photothermal nanotherapy combined with anti-PD-L1 blockade not only eradicated the primary 4T1 tumor but also eliminated metastatic tumor growth (Figure 7J and K) Benefiting from this effective tumor inhibition, half of the mice receiving CuS/EPDA/PD-L1 co-treatment remained alive after 50 days post treatment indicating the immense potential of NCs in cancer therapy.

Discussion

Tregs in metastatic carcinoma play a critical role in the establishment of immunosuppression, which is accountable for tumor relapse and cancer cell chemoresistance.[7,30] This occurs because intratumoral Tregs influence the immunosuppressive TME and their infiltration is negatively correlated with patient survival.[31,32] Recent advances in

nanoparticle-based immune check point inhibitor therapy have improved the anti-tumor immunity against various types of malignancies, including NSCLC.[33–35] Our findings reveal that Tregs immunosuppressive signaling can be restrained in both in vivo and ex vivo by using a CuS/EPDA photothermal nanocarrier model. The combinational use of epacadostat, an inhibitor of immunosuppression and IDO-1 and Dasatinib, a multikinase inhibitor that prevents the proliferation and function of $CD4^+CD25^+$ regulatory cells, shows promising results. The crucial advantage of this CuS-based nanotherapy approach is the immediate co-delivery to the tumor of two agents of different modes of action. Furthermore, copper sulfide NPs have been known to possess exceptional characteristics, like low levels of biotoxicity, high photothermal conversion efficiency, unique molar extinction coefficient and superior NIR optical absorption.[36] Enclosement of epacadostat and Dasatinib in CuS NCs enables the photothermal ablation of tumors, without affecting the surrounding healthy tissues and prompts immune system re-activation. Moreover, epacadostat inhibits IDO-1 activity[31] and can restrain immunosuppression signaling via upregulation of $CD86^+$ dendritic cells and reduction in Treg expression.[37,38] Likewise, Dasatinib blocks Treg's action through inhibition of the tyrosine kinase activities c-KIT, EPHA2, and PDGFRβ involved in tumor progression and metastasis. In addition, it prevents the proliferation and function of $CD4^+CD25^+$ regulatory T cells and their accumulation in the peripheral blood and thus reversing T cell suppression.[18,39] In summary, this study shows that the delivery of elaborately designed nanocatalysts into the tumor tissue can reverse Treg-promoted tumor immunosuppression and reactivate the immune system's mechanisms. CuS/EPDA NCs have quicker release rates and show longer retention time in tumor tissues (Figure 4B), likely due to their biochemical structure.[36,40,41] Taken together, these results reveal the crucial role of Treg-targeted nanoplatform in inhibiting lung immunosuppressive metastasis and will provide additional insights on the development of new cancer immunotherapy regimes for efficient reticence of metastatic neoplasia.

Abbreviations

Tregs, regulatory T cells; DCs, dendritic cells; NCs, nanocarriers; NIR, near infrared; FoxP3, transcription factor fork head box P3; SFKs, SRC family kinases; IDO-1, indoleamine 2,3-dioxygenase-1; PDGF-B, platelet-derived growth factor-subunit B; ^{18}F-FDG, fluorodeoxyglucose F18; AICD, activation-induced cell death; MDSCs, myeloid-derived suppressor cells.

Data Sharing Statement

All relevant data in the article and Supplementary Information are available from the corresponding author upon reasonable request.

Acknowledgments

Author Contributions

All authors made a significant contribution to the work reported, whether that is in the conception, study design, execution, acquisition of data, analysis and interpretation, or in all these areas; took part in drafting, revising or critically reviewing the article; gave final approval of the version to be published; have agreed on the journal to which the article has been submitted; and agree to be accountable for all aspects of the work.

Funding

Disclosure

The authors declare no conflicts of interest in relation to this work.

References

1. Bray F, Ferlay J, Soerjomataram I, Siegel RL, Torre LA, Jemal A. Global cancer statistics 2018:GLOBOCAN estimates of incidence and mortality worldwide for 36 cancers in 185 countries. *CA Cancer J Clin*. 2018;68(6):394–424. doi:10.3322/caac.21492

2. Hirsch FR, Scagliotti GV, Mulshine JL, et al. Lung cancer: current therapies and new targeted treatments. *Lancet*. 2017;389(10066):299–311. doi:10.1016/S0140-6736(16)30958-8

3. Chen DS, Mellman I. Elements of cancer immunity and the cancer-immune set point. *Nature*. 2017;541(7637):321–330. doi:10.1038/nature21349

4. Rahma OE, Hodi FS. The intersection between tumor angiogenesis and immune suppression. *Clin Cancer Res*. 2019;25(18):5449–5457. doi:10.1158/1078-0432.CCR-18-1543

5. Wang RF. Immune suppression by tumor-specific CD4+regulatoryT-cells in cancer. *Semin Cancer Biol*. 2006;16(1):73–79. doi:10.1016/j.semcancer.2005.07.009

6. Dominguez-Villar M, Hafler DA. Regulatory T cells in autoimmune disease. *Nat Immunol*. 2018;19(7):665–673. doi:10.1038/s41590-018-0120-4

7. Togashi Y, Shitara K, Nishikawa H. Regulatory T cells in cancer immunosuppression - implications for anticancer therapy. *Nat Rev Clin Oncol*. 2019;16(6):356–371. doi:10.1038/s41571-019-0175-7

8. Tanaka A, Sakaguchi S. Regulatory T cells in cancer immunotherapy. *Cell Res*. 2017;27(1):109–118. doi:10.1038/cr.2016.151

9. Sadelain M, Rivière I, Riddell S. Therapeutic T cell engineering. *Nature*. 2017;545(7655):423–431. doi:10.1038/nature22395

10. Wing JB, Tanaka A, Sakaguchi S. Human FOXP3(+) regulatory T cell heterogeneity and function in autoimmunity and cancer. *Immunity*. 2019;50(2):302–316. doi:10.1016/j.immuni.2019.01.020

11. Campbell DJ, Koch MA. Phenotypical and functional specialization of FOXP3+regulatory T cells. *Nat Rev Immunol*. 2011;11(2):119–130. doi:10.1038/nri2916

12. Zou W. Regulatory T cells, tumour immunity and immunotherapy. *Nat Rev Immunol*. 2006;6(4):295–307. doi:10.1038/nri1806

13. Kumar BV, Connors TJ, Farber DL. Human T cell development, localization, and function throughout life. *Immunity*. 2018;48(2):202–213. doi:10.1016/j.immuni.2018.01.007

14. Saleh R, Elkord E. FoxP3(+) T regulatory cells in cancer: prognostic biomarkers and therapeutic targets. *Cancer Lett*. 2020;490:174–185. doi:10.1016/j.canlet.2020.07.022

15. Guo X, Zhang Y, Zheng L, et al. Global characterization of T cells in non-small-cell lung cancer by single-cell sequencing. *Nat Med*. 2018;24(7):978–985. doi:10.1038/s41591-018-0045-3

16. Li C, Jiang P, Wei S, Xu X, Wang J. Regulatory T cells in tumor microenvironment: new mechanisms, potential therapeutic strategies and future prospects. *Mol Cancer*. 2020;19(1):116. doi:10.1186/s12943-020-01234-1

17. Lucca LE, Dominguez-Villar M. Modulation of regulatory T cell function and stability by co-inhibitory receptors. *Nat Rev Immunol*. 2020;20(11):680–693. doi:10.1038/s41577-020-0296-3

18. Killock D. Dasatinib versus imatinib in paediatric ALL. *Nat Rev Clin Oncol*. 2020;17(4):197. doi:10.1038/s41571-020-0337-7

19. Gore L, Kearns PR, de Martino ML, et al. Dasatinib in pediatric patients with chronic myeloid leukemia in chronic phase: results from a Phase II trial. *J Clin Oncol*. 2018;36(13):1330–1338. doi:10.1200/JCO.2017.75.9597

20. Haouala A, Widmer N, Duchosal MA, Montemurro M, Buclin T, Decosterd LA. Drug interactions with the tyrosine kinase inhibitors imatinib, dasatinib, and nilotinib. *Blood*. 2011;117(8):e75–87. doi:10.1182/blood-2010-07-294330

21. Paydas S. Dasatinib, large granular lymphocytosis, and pleural effusion: useful or adverse effect? *Crit Rev Oncol Hematol*. 2014;89(2):242–247. doi:10.1016/j.critrevonc.2013.10.005

22. Fei F, Yu Y, Schmitt A, et al. Dasatinib inhibits the proliferation and function of CD4+CD25+ regulatory T cells. *Br J Haematol*. 2009;144(2):195–205. doi:10.1111/j.1365-2141.2008.07433.x

23. Montero JC, Seoane S, Ocaña A, Pandiella A. Inhibition of SRC family kinases and receptor tyrosine kinases by dasatinib: possible combinations in solid tumors. *Clin Cancer Res*. 2011;17(17):5546–5552. doi:10.1158/1078-0432.CCR-10-2616

24. Lowe DB, Bose A, Taylor JL, et al. Dasatinib promotes the expansion of a therapeutically superior T-cell repertoire in response to dendritic cell vaccination against melanoma. *Oncoimmunology*. 2014;3(1):e27589. doi:10.4161/onci.27589

25. Yang Y, Liu C, Peng W, et al. Antitumor T-cell responses contribute to the effects of dasatinibonc-KIT mutant murine mastocytoma and are potentiated by anti-OX40. *Blood*. 2012;120(23):4533–4543. doi:10.1182/blood-2012-02-407163

26. Prendergast GC, Malachowski WP, DuHadaway JB, Muller AJ. Discovery of IDO1 inhibitors: from bench to bedside. *Cancer Res*. 2017;77(24):6795–6811. doi:10.1158/0008-5472.CAN-17-2285

27. Komiya T, Huang CH. Updates in the clinical development of epacadostat and other indoleamine 2,3-Dioxygenase1Inhibitors (IDO1) for human cancers. *Front Oncol*. 2018;8:423. doi:10.3389/fonc.2018.00423

28. Domvri K, Petanidis S, Anestakis D, et al. Exosomal lncRNA PCAT-1 promotes Kras-associated chemoresistance via immunosuppressive miR-182/miR-217 signaling and p27/CDK6 regulation. *Oncotarget*. 2020;11(29):2847–2862. doi:10.18632/oncotarget.27675

29. Domvri K, Petanidis S, Zarogoulidis P, et al. Treg-dependent immunosuppression triggers effector T cell dysfunction via the STING/ILC2 axis. *Clin Immunol*. 2021;222:108620. doi:10.1016/j.clim.2020.108620

30. Ferreira LMR, Muller YD, Bluestone JA, Tang Q. Next-generation regulatory T cell therapy. *Nat Rev Drug Discov*. 2019;18(10):749–769. doi:10.1038/s41573-019-0041-4

31. Marshall EA, Ng KW, Kung SH, Conway EM, Martinez VD, Halvorsen EC. Emerging roles of T helper 17 and regulatory T cells in lung cancer progression and metastasis. *Mol Cancer*. 2016;15(1):67. doi:10.1186/s12943-016-0551-1

32. Kamada T, Togashi Y, Tay C, et al. PD-1(+) regulatory T cells amplified by PD-1 blockade promote hyperprogression of cancer. *Proc Natl Acad Sci USA*. 2019;116(20):9999–10008. doi:10.1073/pnas.1822001116

33. Sanaei MJ, Pourbagheri-Sigaroodi A, Kaveh V, et al. Recent advances in immune checkpoint therapy in non-small cell lung cancer and opportunities for nanoparticle-based therapy. *Eur J Pharmacol*. 2021;909:174404. doi:10.1016/j.ejphar.2021.174404

34. Masoumi E, Tahaghoghi-Hajghorbani S, Jafarzadeh L, Sanaei MJ, Pourbagheri-Sigaroodi A, Bashash D. The application of immune checkpoint blockade in breast cancer and the emerging role of nanoparticle. *J Control Release*. 2021;10(340):168–187.

35. Sanaei MJ, Pourbagheri-Sigaroodi A, Kaveh V, Sheikholeslami SA, Salari S, Bashash D. The application of nano-medicine to overcome the challenges related to immune checkpoint blockades in cancer immunotherapy: recent advances and opportunities. *Crit Rev Oncol Hematol*. 2021;157:103160. doi:10.1016/j.critrevonc.2020.103160

36. Liu Y, Ji M, Wang P. Recent advances in small copper sulfide nanoparticles for molecular imaging and tumor therapy. *Mol Pharm*. 2019;16 (8):3322–3332. doi:10.1021/acs.molpharmaceut.9b00273

37. Labadie BW, Bao R, JJ Luke. Reimagining IDO pathway inhibition in cancer immunotherapy via downstream focus on the tryptophan-kynurenine-aryl hydrocarbon axis. *Clin Cancer Res*. 2019;25(5):1462–1471. doi:10.1158/1078-0432.CCR-18-2882

38. Le Naour J, Galluzzi L, Zitvogel L, Kroemer G, Vacchelli E. Trialwatch: IDO inhibitors in cancer therapy. *Oncoimmunology*. 2020;9(1):1777625. doi:10.1080/2162402X.2020.1777625

39. Cortes JE, Saglio G, Kantarjian HM, et al. Final 5-year study results of DASISION: the dasatinib versus imatinib study in treatment-naive chronic myeloid leukemia patients trial. *J Clin Oncol*. 2016;34(20):2333–2340. doi:10.1200/JCO.2015.64.8899

40. Gao W, Sun Y, Cai M, et al. Copper sulfide nanoparticles as a photothermal switch for TRPV1 signaling to attenuate atherosclerosis. *Nat Commun*. 2018;9(1):231. doi:10.1038/s41467-017-02657-z

41. Wang X, Guo L, Zhang S, et al. Copper sulfide facilitates hepatobiliary clearance of gold nanoparticles through the copper-transporting ATPase ATP7B. *ACS Nano*. 2019;13(5):5720–5730. doi:10.1021/acsnano.9b01154